J. Fluid Mech. (2021), *vol*. 907, A4. © The Author(s), 2020.
Published by Cambridge University Press
doi:10.1017/jfm.2020.816

Axisymmetric evolution of gravity-driven thin films on a small sphere

Jian Qin[1], Yu-Ting Xia[1] and Peng Gao[1,2,†]

[1]Department of Modern Mechanics, University of Science and Technology of China, Hefei, Anhui 230026, PR China

[2]State Key Laboratory of Fire Science, University of Science and Technology of China, Hefei, Anhui 230026, PR China

(Received 1 April 2020; revised 18 September 2020; accepted 22 September 2020)

We study the axisymmetric evolution of a liquid film on a solid sphere governed by gravity, capillarity and viscous forces. The lubrication equations established in spherical coordinates are numerically solved using finite elements and local similarity solutions are obtained. Results show that the evolution behaves differently at early and late stages. At the early stage, the interface evolves in such a way that the capillary effect can be ignored. At the late stage, there emerge four zones from top to bottom: a thin film, a ridge ring, a dimple ring and a pendant drop. Each zone is governed by the balance of different forces, and hence is characterized by an individual physical mechanism. Consequently, the pendant drop is quasi-static, and the film thicknesses of other regions follow different scaling laws. The position of the dimple remains unchanged at the late stage.

Key words: capillary flows, thin films, lubrication theory

1. Introduction

Film evolution on a solid substrate has been studied over the years for its application in cleaning (Parkin & Palgrave 2005), printing (Kumar 2015) and coating (Weinstein & Ruschak 2004) processes encountered in natural and industrial settings.

There have been numerous investigations of film evolution on a flat plate, which especially focused on subjects like dip coating (Blake & Ruschak 1979; Snoeijer *et al.* 2007; Gao *et al.* 2016), spin coating (Emslie, Bonner & Peck 1958; Wilson, Hunt & Duffy 2000), drop spreading (Tanner 1979; Hocking 1983) and sliding (Benilov & Benilov 2015). As a further complexity, the effects of curved substrates (cylinders in particular) have been included, e.g. coating films outside a horizontal or vertical cylinder (Reisfeld & Bankoff 1992; Quéré 1999), and rimming flows inside or outside a rotating cylinder (Benilov, Benilov & Kopteva 2008; Lopes, Thiele & Hazel 2018). Models for other geometries of walls have been established as well (Schwartz & Weidner 1995; Myers, Charpin & Chapman 2002; Roy, Roberts & Simpson 2002; Howell 2003), including film flows over topography (Stillwagon & Larson 1988; Kalliadasis, Bielarz & Homsy 2000), lubrication at a corner (Stocker & Hosoi 2005) and films on a sphere, on which we focus in this paper.

† Email address for correspondence: gaopeng@ustc.edu.cn

Coating flows on a sphere have intrigued researchers in recent years. The impact of a droplet on a solid sphere often leads to a liquid film on the sphere, where inertia dominates the evolution at the early stage and viscosity takes over at the late stage (Bakshi, Roisman & Tropea 2007). The wetting dynamics accompanied by the advancing contact line plays an important role in the formation of liquid films (Zhu *et al.* 2017). In the condition of continuous liquid supply, Wild & Potter (1972) and Belousov & Belousov (2010) experimentally measured the film thickness on a sphere. In contrast, for cases without liquid supply, film evolution was explored more theoretically. Takagi & Huppert (2010) established a lubrication equation on a spherical surface in the presence of gravity. Treating the film around the top of the sphere (the 'north pole') as a uniform one, they obtained the film thickness which decreases as $t^{-1/2}$, where t is time. As for the non-uniform effect, Lee *et al.* (2016) derived an asymptotic solution around the north pole, consistent with their experimental results. Kang, Nadim & Chugunova (2016) considered centrifugal effects and studied the dynamics of films on a rotating sphere, where they discovered three different steady states. Then they established a three-dimensional model to explore the Marangoni effect induced by temperature gradient (Kang, Nadim & Chugunova 2017). Film evolution on a sphere can also be employed as a model to study tear film dynamics (Braun *et al.* 2012). As for the inner surface of a sphere, a model was built by Balestra, Nguyen & Gallaire (2018) who explored Rayleigh–Taylor instability of coating films inside a spherical shell.

Even though it is a fundamental problem as to how a film evolves on a sphere, we point out that there still remain some crucial problems to be solved, including a proper description of local evolution and a rational physical interpretation. In this work, we focus on film evolution on a sphere under the influences of gravity, viscous force and capillarity, and the work is performed under the assumption of axisymmetry. The governing equation for the present problem is a special case of Kang *et al.* (2016), under the condition of zero rotation speed. The difference between Kang *et al.* (2016) and the present work is that they mainly focused on the different types of steady states, while we are interested in the time evolution and scaling laws followed by local interfacial structures. According to our results, distinct features exist at early and late stages of the evolution. In particular, four physically different zones emerge at the late stage, where we make a detailed description and analysis of the results and hope that our work can help understand coating films on curved substrates.

The paper is organized as follows. In § 2, we present the mathematical description of our problem, which contains gravity, capillarity and viscous force. In § 3, the problem is solved both numerically and analytically to illustrate the whole process of film evolution. We show the behaviour of the film at early and late stages, present distinct regimes and scaling laws in different regions at the late stage and perform a parametric study. All our analyses are consistent with the numerical results. In § 4, we provide a conclusion to our results.

2. Formulation

Consider an axisymmetric liquid film on a sphere (figure 1). Initially, the film has a uniform thickness h_0, which is assumed much smaller than the radius of the solid sphere R, i.e. $\delta = h_0/R \ll 1$. Gravity is along the symmetric axis, with g the gravitational acceleration. The liquid density is denoted by ρ, and the viscous and capillary forces are characterized by the liquid viscosity μ and the surface tension σ, respectively. According to estimation in Kang *et al.* (2016), the Reynolds number is $Re \sim O(\delta^2)$, meaning that

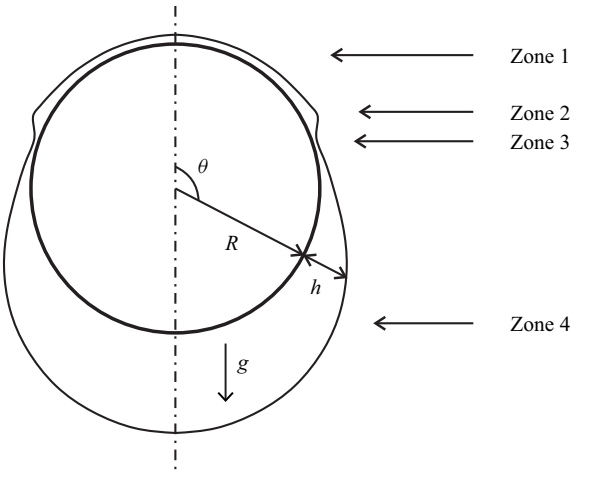

FIGURE 1. Sketch of interface morphology at the late stage of evolution. Zone 1: a thin film; zone 2: a ridge ring; zone 3: a dimple ring; zone 4: a pendant drop.

inertial effects can be safely ignored in our work. In this way, the evolution of the film thickness h is dominated by gravity, viscosity and capillarity. We adopt the spherical coordinate system (r, θ, ϕ), indicating the radial distance, polar angle and azimuthal angle, respectively. The curvature of the interface rescaled by h_0/R^2 can be written as

$$\kappa = \frac{\delta(1+\delta H)(\partial^2 H/\partial\theta^2) - 3\delta^2(\partial H/\partial\theta)^2 - 2(1+\delta H)^2}{\delta[(1+\delta H)^2 + \delta^2(\partial H/\partial\theta)^2]^{3/2}} + \frac{(\partial H/\partial\theta)\cot\theta}{(1+\delta H)[(1+\delta H)^2 + \delta^2(\partial H/\partial\theta)^2]^{1/2}}, \tag{2.1}$$

where $H = h/h_0$ is the rescaled film thickness. We can expand the curvature in terms of the small parameter δ,

$$\kappa = -\frac{2}{\delta} + K + O(\delta), \tag{2.2}$$

where $-2/\delta$ denotes the constant part of the curvature, which is equal to that of the solid sphere and does not drive a flow, and

$$K = 2H + \frac{1}{\sin\theta}\frac{\partial}{\partial\theta}\left(\sin\theta\frac{\partial H}{\partial\theta}\right) \tag{2.3}$$

is the variable part that generates capillary pressure gradient.

Following Kang *et al.* (2016), we have the following lubrication equation to describe our problem:

$$\frac{\partial H}{\partial\tau} + \frac{1}{\sin\theta}\frac{\partial}{\partial\theta}\left[H^3\sin\theta\left(Bo^{-1}\frac{\partial K}{\partial\theta} + \sin\theta\right)\right] = 0, \tag{2.4}$$

where

$$\tau = \frac{\rho g h_0^2 t}{3\mu R}, \quad Bo = \frac{\rho g R^3}{\sigma h_0}. \tag{2.5a,b}$$

Here Bo is the Bond number, representing the ratio of gravity to capillary forces. The effects of capillarity and gravity are represented, respectively, by the two terms

within parentheses in equation (2.4). The small parameter δ disappears under lubrication approximation, and thus the only remaining parameter in our problem is Bo. Note that only the effect of the tangential gravity component is retained in the lubrication equation, while the other component perpendicular to the wall has been neglected since it is of $O(\delta)$ (Balestra *et al.* 2018). We have verified that, for the considered values of Bo, the neglect of the tangential gravity component as well as higher-order terms of curvature does not show appreciable differences.

According to symmetry, we have the following boundary conditions:

$$\left.\begin{aligned} \left.\frac{\partial H}{\partial \theta}\right|_{\theta=0} &= \left.\frac{\partial H}{\partial \theta}\right|_{\theta=\pi} = 0, \\ \left.\frac{\partial K}{\partial \theta}\right|_{\theta=0} &= \left.\frac{\partial K}{\partial \theta}\right|_{\theta=\pi} = 0. \end{aligned}\right\} \tag{2.6}$$

The initial uniform film leads to

$$H|_{\tau=0} = 1. \tag{2.7}$$

We employ the finite element method to solve (2.4) together with (2.6) and (2.7). The weak form is written as

$$\left.\begin{aligned} \int_0^{\pi} \left[\frac{\partial H}{\partial \tau} u - H^3 \left(Bo^{-1}\frac{\partial K}{\partial \theta} + \sin\theta\right)\frac{\partial u}{\partial \theta}\right] \sin\theta \,\mathrm{d}\theta = 0, \\ \int_0^{\pi} \left[(K - 2H)v + \frac{\partial H}{\partial \theta}\frac{\partial v}{\partial \theta}\right] \sin\theta \,\mathrm{d}\theta = 0, \end{aligned}\right\} \tag{2.8}$$

where u and v are test functions. The weak form is regular, which means the $(\sin\theta)^{-1}$ singularity at both poles in (2.4) is formal and does not really exist. The calculation was performed using FreeFem++ (Hecht 2012), similar to that employed in Xia, Qin & Gao (2020*a*) and Xia, Qin & Mu (2020*b*). The lubrication equation was solved using the finite element method. The nonlinear term was handled by Newton's iteration, and the first-order implicit scheme was used for time integration. We adopted elements of uniform size and constant time steps, which were sufficiently small such that the produced results were converged in a way that the errors cannot be identified by the naked eye. A typical test of mesh convergence is shown in the inset of figure 2(*b*). The results presented below were obtained using 10 000 elements for sufficient accuracy.

The problem can be formally simplified under the transformation

$$z = \cos\theta, \tag{2.9}$$

representing the axis position scaled by R. In particular, at the north pole, we have $\theta = 0, z = 1$, and the south pole corresponds to $\theta = \pi, z = -1$. In this way, (2.4) can be written as

$$\left.\begin{aligned} \frac{\partial H}{\partial \tau} + \frac{\partial}{\partial z}\left\{H^3\left[Bo^{-1}\frac{\partial F}{\partial z} - (1 - z^2)\right]\right\} = 0, \\ F = (1 - z^2)^2 \frac{\partial^2 H}{\partial z^2}. \end{aligned}\right\} \tag{2.10}$$

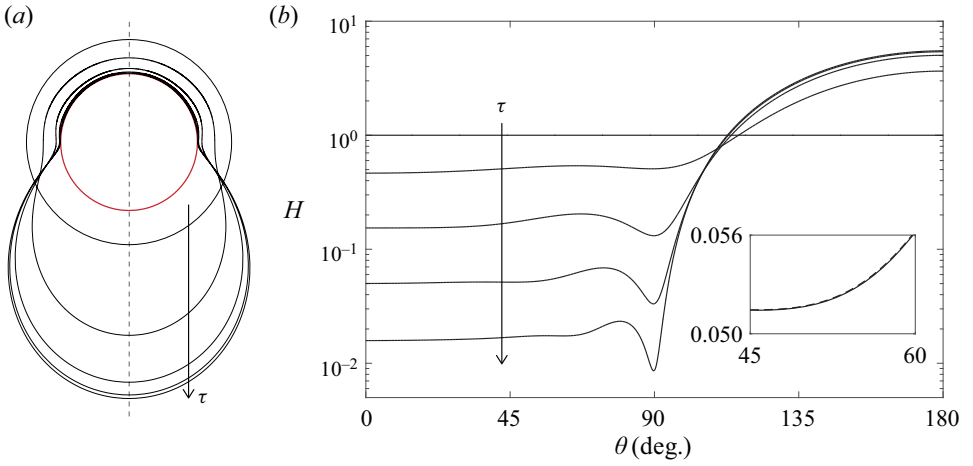

FIGURE 2. Interface evolution for $Bo = 24$ at $\tau = 0, 1, 10, 100, 1000$. (*a*) The polar plot, where the ratio of the radius of the sphere to the film thickness has been multiplied by $2h_0/R$ for a better view. (*b*) The Cartesian plot with the film thickness H in logarithmic scale. The inset illustrates the mesh independence at $\tau = 100$, where the dashed and solid lines correspond to 5000 and 10 000 elements, respectively.

It is trivial by integrating (2.4) and (2.10) to prove that the volume conservation is satisfied automatically:

$$\int_0^{\pi} H \sin\theta \, \mathrm{d}\theta = \int_{-1}^{1} H \, \mathrm{d}z = 2. \tag{2.11}$$

Equation (2.10) is more convenient for us to analyse the problem. Not only is the transformed problem more concise, but also the formal $(\sin\theta)^{-1}$ singularity at both poles in the original equation is resolved. For convenience, we define a function $Q(\tau, z)$ to replace the term within the braces in (2.10):

$$Q(\tau, z) = H^3 \left[Bo^{-1} \frac{\partial F}{\partial z} - (1 - z^2) \right]. \tag{2.12}$$

Physically, Q represents the volume flow rate through a cross-section of constant z.

3. Results

3.1. *Overview of film evolution*

We begin with an overview of film evolution dominated by the combined work of gravity, capillarity and viscous force. The film evolution is shown in figure 2 for $Bo = 24$. The value $Bo = 24$ is chosen such that the dimple locates at the equator, which is demonstrated in § 3.3.2. It will be shown that the evolution behaves differently at early and late stages.

At the early stage, the gradient of capillary pressure is weak due to the given initial condition, and the evolution is primarily driven by gravity and resisted by viscous force. As time increases to the late stage, the film splits into four distinct zones (figure 1). The characteristic length of the film varies at each zone, which is consequently governed by different forces. Figure 2 shows that the liquid always accumulates towards the south pole under gravity and eventually forms a pendant drop (zone 4), with its shape hardly varying

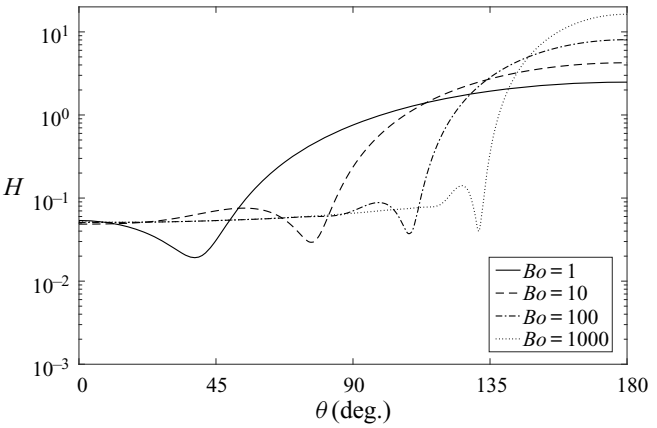

FIGURE 3. Film thickness for different Bond numbers at $\tau = 100$.

with time. This pendant drop is a reflection of hydrostatics, under the balance between gravity and capillary force. At the boundary of the pendant drop there is an apparent contact line, the position of which is constrained by the requirement of a vanishing apparent contact angle due to the connection with a thin film. The thickness of the thin film in zone 1 decreases with time and weakly depends on θ. Capillary pressure gradient can be neglected here due to the small variation of the interfacial curvature, and the viscous flow is driven primarily by gravity, showing a concise scaling law. The connection between zone 1 and zone 4 is characterized by a ridge ring (zone 2) and a dimple ring (zone 3). The dimple ring is formed by capillary force and viscous force, while gravity can be neglected due to the small length scale. The ridge ring is determined by all three forces. Both zones 2 and 3 become thinner and more localized, and eventually give rise to a singularity in the capillary pressure gradient as $\tau \to +\infty$ in zone 3. As presented in the following sections, while zone 4 is quasi-static, the other three zones follow different scaling laws.

As shown in figure 3, the effects of Bo are mainly on the location of the dimple ring and the width of the pendant drop. A larger Bo results in a narrower pendant drop and a wider flat film, whose thickness, however, is almost independent of Bo.

3.2. *Early-stage evolution*

At the early stage, the interface configuration is close to the initial spherical shape, which means the curvature barely changes along the interface. We assume Bo^{-1} is no more than $O(1)$, then write $H = 1 + f_1(z)\tau + f_2(z)\tau^2 + O(\tau^3)$ and substitute it into (2.10). Finally we obtain

$$H = 1 - 2z\tau + 3(3z^2 - 1)\tau^2 + O(\tau^3). \tag{3.1}$$

This indicates that the early-stage evolution is independent of Bo, which is a manifestation of the absence of capillary pressure gradient. Figure 4 displays the shape of the interface at the early stage. The film thickness has been transformed so that the range is of $O(1)$. We can see that there is almost no difference between (3.1) and the full numerical solution at the early stage. In figure 5 we display the evolution of the film thickness at the north pole, where (3.1) is confirmed to be valid at the early stage.

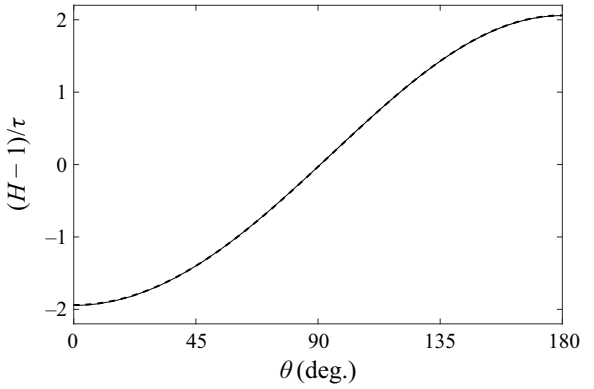

FIGURE 4. Interface configuration for $Bo = 1$ at $\tau = 0.01$. Solid line: numerical solution of (2.4); dashed line: (3.1).

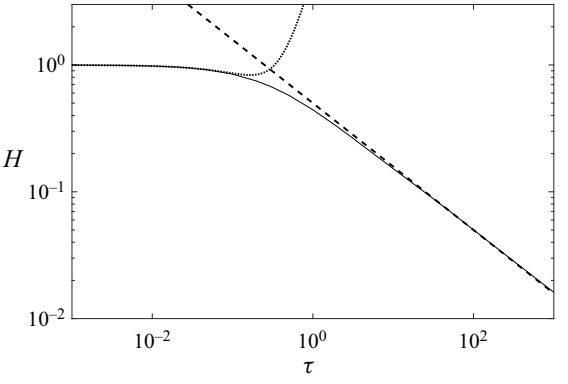

FIGURE 5. Film thickness at the north pole for $Bo = 24$. Solid line: numerical solution of (2.4); dotted line: early-stage evolution (3.1), where the capillary pressure gradient can be neglected; dashed line: late-stage evolution (3.7).

3.3. *Late-stage evolution: four-zone regime*

As discussed in § 3.1, the governing equations can be simplified due to the appropriate neglecting of capillary or gravitational force. Accordingly, the film evolution in different zones can be studied in a piecewise way, and may admit local self-similarity solutions and scaling laws. The exponents of the scaling laws can be obtained by matching the solutions in different zones.

3.3.1. *Zone 1: thin film*

From figure 3 we see that the thickness of the film around the north pole only varies slightly such that capillary forces can be neglected, which will be validated later, and (2.10) can be written as

$$\frac{\partial H}{\partial \tau} - \frac{\partial}{\partial z}\left[H^3\left(1 - z^2\right)\right] = 0. \tag{3.2}$$

This equation has a self-similar solution

$$H(z, \tau) = \eta(z)\tau^{-1/2}, \tag{3.3}$$

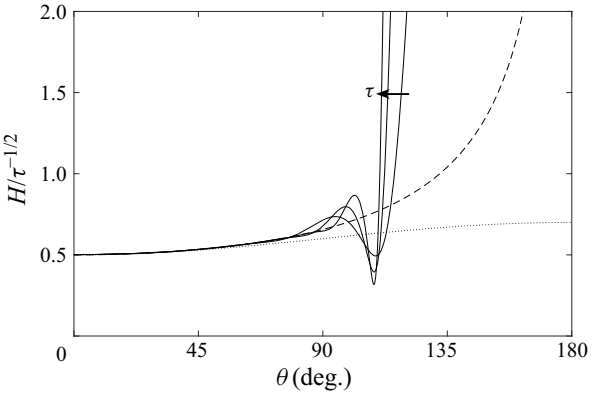

FIGURE 6. Rescaled film thickness for $Bo = 100$ at $\tau = 10, 100, 1000$ (solid lines). The dashed and dotted lines represent (3.5*a*,*b*) and (3.6), respectively.

where $\eta(z)$ satisfies the following ordinary differential equation:

$$\tfrac{1}{2}\eta + \left[\eta^3\left(1-z^2\right)\right]' = 0, \tag{3.4}$$

where a prime denotes the derivative with respect to z.

Furthermore, the exact solution of (3.4) under the constraint $|\eta'(1)| < +\infty$ is

$$\eta(z) = \frac{[\varphi(1)-\varphi(z)]^{1/2}}{\left(1-z^2\right)^{1/3}}, \quad \varphi(z) \equiv \frac{z}{3}{}_2F_1\left(\frac{1}{3}, \frac{1}{2}; \frac{3}{2}; z^2\right), \tag{3.5a,b}$$

where ${}_2F_1$ is the hypergeometric function. This solution is monotonic in z (dashed line in figure 6). The monotonic behaviour is a manifestation of the fact that the film drained by gravity becomes thicker in the flow direction. Similar behaviours occur in falling films along a vertical wall (de Gennes, Brochard-Wyart & Quéré 2004). The film configuration was previously described by Lee *et al.* (2016) and Balestra *et al.* (2018) as

$$\eta(z) = \tfrac{1}{2} + \tfrac{1}{10}(1-z) + O((1-z)^2), \tag{3.6}$$

which is a truncated version of (3.5*a*,*b*) and is valid for small $1-z$, while (3.5*a*,*b*) remains precise throughout zone 1.

In particular, we have $\eta(1) = 1/2$ at the north pole, corresponding to

$$H|_{z=1} = \tfrac{1}{2}\tau^{-1/2}, \quad \tau \to +\infty. \tag{3.7}$$

This result has been previously obtained by Takagi & Huppert (2010), and is the same as the late-stage result of a drop impacting on a sphere (Bakshi *et al.* 2007).

The statement that capillarity can be neglected is validated by checking the flow rate (2.12). The capillary flow rate decays as

$$Bo^{-1}H^3\frac{\partial}{\partial z}\left[(1-z^2)^2\frac{\partial^2 H}{\partial z^2}\right] \propto \tau^{-2}, \tag{3.8}$$

faster than the gravitational flow rate which is $H^3(1-z^2) \propto \tau^{-3/2}$. This means that capillarity can be neglected in zone 1.

In figure 6, our theory is compared with numerical solution at three different times at the late stage. These shapes collapse well throughout this region, confirming the similarity solution (3.3). As shown in the figure, our prediction of the film configuration (3.5*a*,*b*) is more precise than that in Lee *et al.* (2016) and Balestra *et al.* (2018). The profile at lower position of the sphere cannot be described by the capillarity-free theory, as it serves as a reflection of capillarity to be discussed below.

3.3.2. *Zone 4: pendant drop*

At late times of the evolution, the film on the lower body of the sphere is quasi-static, forming a pendant drop. This zone is essentially the same as the solution of steady states without rotation, as reported by Kang *et al.* (2016), but with coefficients not provided explicitly in their formula. Here we present a fully analytical solution of the pendant drop. In this region, capillary force is balanced with gravity. Since the flow within the static pendant drop can be ignored, we set $Q = 0$ in (2.12) and obtain a third-order ordinary equation for $H(z)$:

$$Bo^{-1}\frac{\mathrm{d}}{\mathrm{d}z}\left[\left(1-z^2\right)^2\frac{\mathrm{d}^2H}{\mathrm{d}z^2}\right]-\left(1-z^2\right)=0. \tag{3.9}$$

Three boundary conditions are needed. If we use z_d to represent the position of the dimple ring (to be determined in the following), the extremely thin film here is seen as an apparent contact line, and thus leads to

$$H(z_d)=0. \tag{3.10}$$

Since the film here is connected to the film upwards, the apparent contact line should be accompanied with a vanishing apparent contact angle:

$$H'(z_d)=0. \tag{3.11}$$

At the bottom of the pendant drop, we have the third condition from (2.6), which in terms of z is

$$\sqrt{1-z^2}H'(z)\Big|_{z=-1}=0. \tag{3.12}$$

The solution to the problem (3.9)–(3.12) is

$$H=\frac{Bo}{3}\left(z_d\frac{z_d-z}{1-z_d}+z\ln\frac{1-z_d}{1-z}\right). \tag{3.13}$$

An extra condition is needed to determine z_d. Since the film thickness in zones 1, 2 and 3 tends to vanish as $\tau\to+\infty$, zone 4 will finally contain the entire liquid, and the volume conservation (2.11) becomes

$$\int_{-1}^{z_d}H\,\mathrm{d}z=2, \tag{3.14}$$

which yields that Bo and z_d (or θ_d) are dependent on each other:

$$Bo=\frac{24(1-z_d)}{(1+z_d)^3}=\frac{24(1-\cos\theta_d)}{(1+\cos\theta_d)^3}. \tag{3.15}$$

It is trivial to confirm that $\mathrm{d}^2H/\mathrm{d}\theta^2$ is positive at $z=z_d$ and negative at $z=-1$. Therefore, there must be an inflection point within this region.

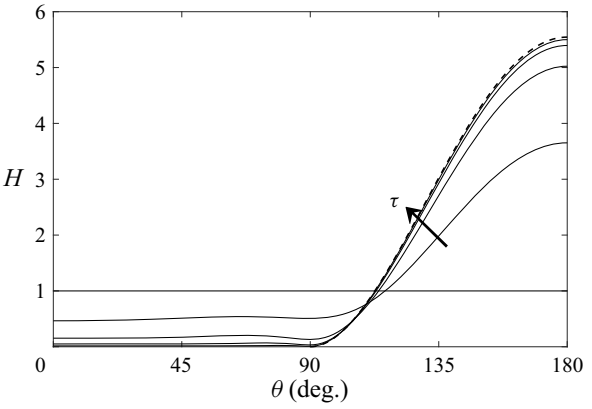

FIGURE 7. Interface evolution for $Bo = 24$. Solid lines represent solutions at $\tau = 0, 1, 10, 100, 1000$. The dashed line displays our analytical solution (3.13).

When time approaches infinity, our numerical result in zone 4 has a limit which is exactly given by (3.13) (figure 7). Correspondingly, (3.15) predicts the final position of the dimple ring. Figure 8 shows that this prediction is fairly precise. As we see, the larger the value of Bo, the lower is the dimple ring. In particular, when $Bo = 24$, we have $z_d = 0$, which means the dimple ring is located on the equator of the sphere.

3.3.3. *Zone 3: dimple ring*

Unlike zone 1 and zone 4, this zone is dominated by capillary and viscous forces, and gravity is neglected (validated later), similar to the 'pinch region' proposed by Lamstaes & Eggers (2017). The width across the dimple ring is much smaller than the circumference of the sphere, expressed as $|z - z_d| \ll 1$. Not only the film thickness but also the width of the zone is decreasing, and this decreasing is believed to be self-similar since there is no characteristic length within this region. For our problem, this decreasing can be measured by flow current. Integrating (2.10) throughout zone 1, i.e. from $z = 1$ to $z = z_d$, and using (3.3), we obtain

$$Q(\tau, z_d) = -\int_1^{z_d} \frac{\partial H}{\partial \tau}\,\mathrm{d}z = \frac{1}{2}\tau^{-3/2}\int_1^{z_d} \eta(z)\,\mathrm{d}z. \tag{3.16}$$

Here we have neglected the flow rate variation in zone 2, which will be estimated as $O(\tau^{-8/5})$ based on (3.35*a*,*b*) and decays faster than (3.16). On the other hand, within zone 3, the function $Q(\tau, z)$ would be

$$Q(\tau, z) = Bo^{-1}H^3\frac{\partial}{\partial z}\left[\left(1 - z^2\right)^2\frac{\partial^2 H}{\partial z^2}\right], \tag{3.17}$$

where gravity has been neglected. Since zone 3 is narrow, i.e. $z \approx z_d$, we have

$$Q(\tau, z_d) \approx Bo^{-1}\left(1 - z_d^2\right)^2 H^3\frac{\partial^3 H}{\partial z^3}, \tag{3.18}$$

where the term $\partial^2 H/\partial z^2$ has been neglected since $|z - z_d| \ll 1$ leads to $|\partial^2 H/\partial z^2| \ll |\partial^3 H/\partial z^3|$.

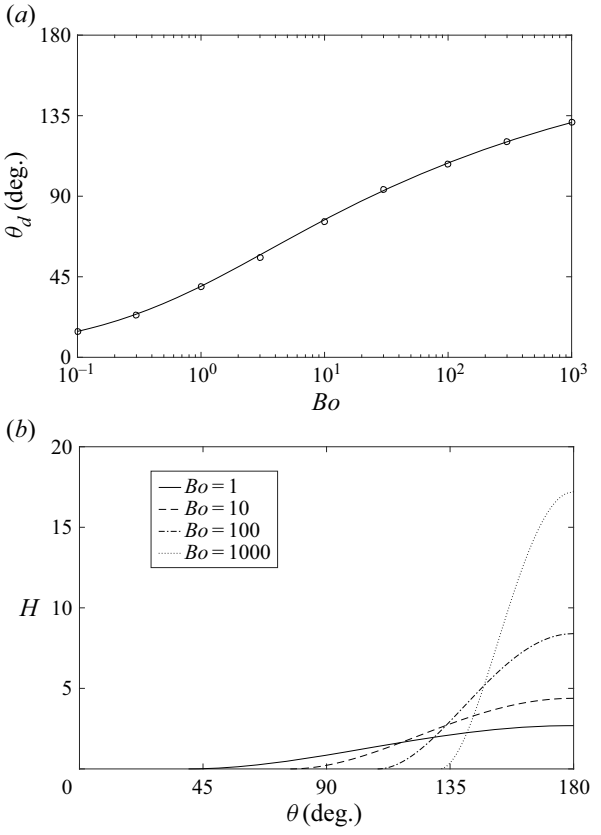

FIGURE 8. (*a*) Position of dimple (the first minimum from the bottom of the sphere) at $\tau = 100$. Circles: numerical solution of (2.4); solid line: (3.15). (*b*) Effect of *Bo* on the profile of the pendant drop.

Combining (3.16) and (3.18), we obtain the well-known 'current equation' (valid only in zone 3):

$$H^3 \frac{\partial^3 H}{\partial z^3} = J(\tau), \tag{3.19}$$

where $J(\tau) = -C\tau^{-3/2}$ and according to (3.15) and (3.16) C is

$$C = \frac{12}{(1+z_d)^5 (1-z_d)^2} \int_{z_d}^{1} \eta(z)\, \mathrm{d}z. \tag{3.20}$$

Different forms of $J(\tau)$ have emerged in other problems (Dupont *et al.* 1993; Lamstaes & Eggers 2017; van Limbeek *et al.* 2019).

From (3.20) we see that C is always positive and only depends on z_d (or *Bo*). As shown in figure 9, C has a minimum $C_{min} \approx 1.449$ at $Bo \approx 1.644$. In addition, for small and large values of *Bo* we have

$$\left.\begin{aligned} C &\sim \frac{9}{16Bo}, \quad Bo \to 0^+, \\ C &\sim 4.805 \left(\frac{Bo}{48}\right)^{5/3}, \quad Bo \to +\infty, \end{aligned}\right\} \tag{3.21}$$

after analysis.

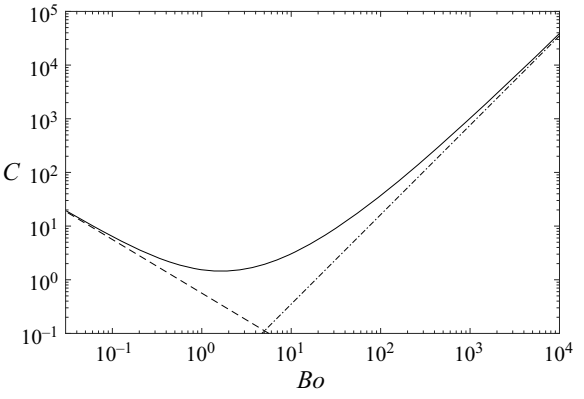

FIGURE 9. Relation between C and Bo (solid line). Dashed and dash-dotted lines represent the asymptotics (3.21).

Now we explore self-similarity of (3.19) by choosing variables

$$\psi(\xi) = \frac{H}{\tau^{\alpha}}, \quad \xi = \frac{z_d - z}{\tau^{\beta}}, \tag{3.22a,b}$$

where we anticipate both α and β to be negative for the local shrinking behaviour. In this way, the flow current will be

$$-C\tau^{-3/2} = J(\tau) = H^3\frac{\partial^3 H}{\partial z^3} = -\psi^3\psi'''\tau^{-4\alpha+3\beta}. \tag{3.23}$$

The presence of similarity solution requires

$$-4\alpha + 3\beta = -\tfrac{3}{2}, \tag{3.24}$$

and the self-similar equation becomes

$$\psi^3\psi''' = C. \tag{3.25}$$

The asymptotic analysis to (3.25) shows $\psi''(\xi)$ approaches a non-negative constant when $|\xi| \to +\infty$ (Lamstaes & Eggers 2017). Approaching zone 4 corresponds to taking the limit $\xi \to +\infty$. The slope angle is zero and the curvature is approximately constant when approaching the apparent contact line, i.e. $z \to z_d^-$. The Taylor expansion of (3.13) is

$$H|_{z\to z_d^-} = \frac{4(2-z_d)}{(1+z_d)^3(1-z_d)}(z-z_d)^2 + O((z-z_d)^3). \tag{3.26}$$

Matching between zone 3 and zone 4 requires

$$\left.\frac{\mathrm{d}^2\psi}{\mathrm{d}\xi^2}\right|_{\xi\to+\infty}\tau^{\alpha-2\beta} = \left.\frac{\mathrm{d}^2 H}{\mathrm{d}z^2}\right|_{z\to z_d^-}. \tag{3.27}$$

This matching condition leads to the second relation between α and β:

$$\alpha - 2\beta = 0. \tag{3.28}$$

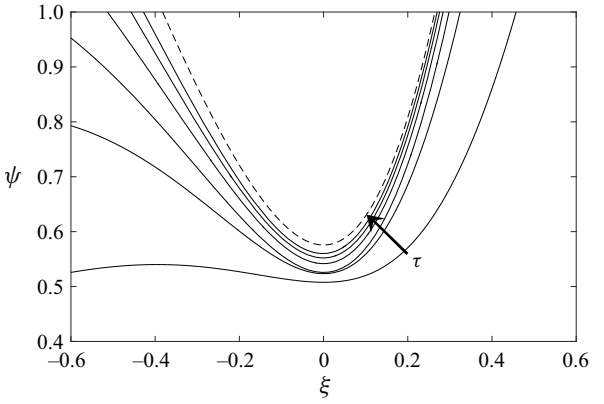

FIGURE 10. Self-similar configuration of the dimple ring. Solid lines represent numerical solutions of (2.4) at $\tau = 1, 10, \ldots, 10^5$ for $Bo = 24$, and the dashed line represents the numerical solution to (3.25) in the limit $\tau \to +\infty$. The arrow points in the direction of increasing τ.

The result after combining (3.24) with (3.28) is

$$\alpha = -3/5, \quad \beta = -3/10. \tag{3.29a,b}$$

So under the definition of

$$\psi = \frac{H}{\tau^{-3/5}}, \quad \xi = \frac{z_d - z}{\tau^{-3/10}}, \tag{3.30a,b}$$

the scaled interface profile $\psi(\xi)$ would be approximately unchanged through time when $\tau \to +\infty$ (figure 10). Note that the limit configuration is not thought to exist physically because a circle of contact line will finally emerge.

It can be easily inferred from (3.30*a*,*b*) that $\partial^3 H/\partial z^3 \propto \tau^{3/10}$ and diverges as $\tau \to +\infty$, corresponding to a singularity of the capillary pressure gradient; $\partial H/\partial z$ and $\partial^2 H/\partial z^2$ remain regular. In particular, we have $\partial H/\partial z \propto \tau^{-3/10}$, indicating that the flow within the dimple can be treated as a parallel shear flow and lubrication approximation still holds. Furthermore, according to (3.30*a*,*b*), the neglected part of the flow rate generated by gravity in (2.12) is approximately $H^3(1 - z_d^2) \propto \tau^{-9/5}$, which is small compared to the capillary part $Bo^{-1}(1 - z_d^2)^2 H^3(\partial^3 H/\partial z^3) \propto \tau^{-3/2}$, justifying the neglect of gravity at the beginning of this subsection.

The final shape of the dimple can be obtained by solving (3.25), which is much easier to solve than the original lubrication equation (2.4). The solution can be determined by imposing the following constraints:

$$\left.\begin{aligned} \psi''(+\infty) &= \frac{8(2 - z_d)}{(1 + z_d)^3(1 - z_d)}, \\ \psi''(-\infty) &= 0, \\ \psi'(0) &= 0. \end{aligned}\right\} \tag{3.31}$$

The first condition is due to (3.27), and the second condition will be checked at the end of § 3.3.4. The proposal of these two conditions is similar to that of earlier researchers (Lamstaes & Eggers 2017; van Limbeek *et al.* 2019). The remaining condition defines the position of the local minimum. Under these constraints, the solution to (3.25) for $Bo = 24$ is obtained numerically and displayed as the dashed line in figure 10, where the shape of the dimple ring approaches the dashed line as τ increases.

3.3.4. *Zone 2: ridge ring*

Although the matching of the flow current between zone 1 and zone 3 works, we point out that the interface configuration does not match because of the different signs of $\partial H/\partial z$ in zone 1 and at the upper part of zone 3, which leads to the existence of zone 2, the ridge ring. In this narrow transition zone, all three forces are believed to be important. The position of the ridge ring moves down approaching zone 3, and the local configuration of the ridge ring keeps narrowing. According to our results, we have $z_r - z_d \to 0$ as $\tau \to +\infty$, where z_r is the position of the peak of the ridge. Under the condition $|z - z_d| \ll 1$, we have

$$Bo^{-1}\left(1 - z_d^2\right)^2 \frac{\partial^3 H}{\partial z^3} = \frac{Q(\tau; z_d)}{H^3} + \left(1 - z_d^2\right), \tag{3.32}$$

according to (2.12). It is confirmed that (3.32) can describe zone 1 by removing the term of capillarity (left-hand side) and zone 3 by eliminating the term of gravity (last term on the right-hand side). Similar to the 'bump' explored in van Limbeek *et al.* (2019), the slopes in zones 2 and 3 should match:

$$\frac{H_r}{z_r - z_d} \sim \left[\frac{\partial H}{\partial z}\right]_{zone\ 3} \propto \tau^{-3/10}, \tag{3.33}$$

where H_r is the height of the peak of the ridge. The term $H_r/(z_r - z_d)$ denotes the characteristic slope of the ridge, and $[\partial H/\partial z]_{zone\ 3}$ is the slope in zone 3 and can be estimated according to (3.30*a*,*b*).

On the other hand, all three terms in (3.32) should be of the same order in zone 2. The balance between the first and the third terms yields

$$\frac{H_r}{(z_r - z_d)^3} \sim \left[\frac{\partial^3 H}{\partial z^3}\right]_{zone\ 2} \propto \tau^0. \tag{3.34}$$

Comparing (3.33) and (3.34), we obtain a self-similar scaling law of the ridge evolution (figure 11):

$$z_r - z_d \propto \tau^{-3/20}, \quad H_r \propto \tau^{-9/20}. \tag{3.35a,b}$$

In this way, the curvature will be proportional to $\tau^{-3/20}$ and diminish when time approaches infinity, which justifies the second condition in (3.31).

According to (3.35*a*,*b*), the film thickness in zone 2 declines slower than in zone 1 and zone 3, which reconfirms the ridge ring emerging here. As a transition zone, the ridge ring makes it possible to match zone 1 and zone 3. The connection between the slowest and fastest declining rates in zone 2 and zone 3, respectively, forms an evident local fluctuation between the relatively smooth structures in zone 1 and zone 4.

4. Conclusion and discussion

We have investigated the axisymmetric evolution of gravity-driven films on a solid sphere. The roles of gravity, capillarity and viscous force have been included and examined.

Our results show that film evolution displays different features at early and late stages. At the early stage, the capillary contribution is weak because the film surface is close to a sphere, as imposed by the initial condition. At the late stage, the film between north and south poles splits into four zones. At the top of the sphere (zone 1), the evolution is driven

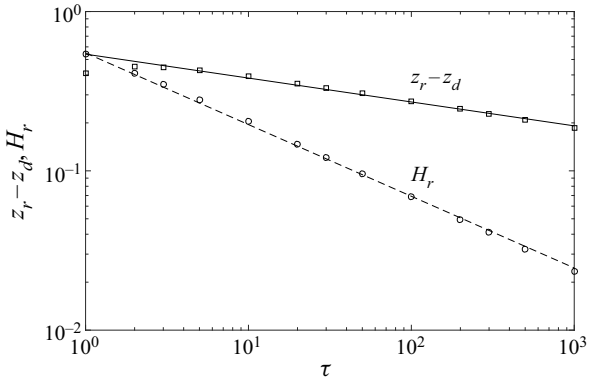

FIGURE 11. Self-similar evolution of the ridge for $Bo = 24$. Symbols represent the numerical solution of (2.4) and lines indicate the scaling law (3.35*a*,*b*).

by gravity and resisted by viscosity, forming a thin flat film with a scaling law of $H \propto \tau^{-1/2}$. At the bottom of the sphere (zone 4), there is a quasi-static pendant drop formed by the balance of gravity and capillarity. The interface of the pendant drop approaches the solid wall by a dimple ring (zone 3), or an apparent contact line, with a vanishing apparent contact angle. As a result, the position of the dimple ring depends on Bo, described by (3.15). While the dimple ring is thinning at a faster rate than the thin film, the mismatch between these two regions leads to a local ridge ring, where all three forces are important. Results show that the ridge ring retains a local maximum film thickness, which decreases slower than both the thin film and the dimple ring.

Similar connection between a flat film and a quasi-static structure appears in other flow geometries. In the dip-coating problem (Gao *et al.* 2016) for example, just above the critical plate speed of wetting transition, there is a dimple located above the static meniscus with a zero apparent contact angle (Snoeijer *et al.* 2008), and the gravity-driven film at the top meets the dimple with a local ridge (Benilov *et al.* 2010). Other problems containing similar order of connection include a thin drop sliding down an inclined plate (Benilov & Benilov 2015), a gas film below a Leidenfrost drop (van Limbeek *et al.* 2019), a bubble rising in a narrow tube (Lamstaes & Eggers 2017), dewetting fronts (Snoeijer & Eggers 2010) and capillary ripples (Jalaal, Seyfert & Snoeijer 2019) in lubrication flows. This seems to be a general pattern of the distribution of film structures, though the scaling laws depend on the specific geometry of each problem.

One way to extend our work is to explore the evolution after a contact line (Bonn *et al.* 2009; Snoeijer & Andreotti 2013) emerges in zone 3, which will lead to film retraction in both zone 1 and zone 4 for a finite equilibrium contact angle. To simulate this process, one should introduce models to capture the formation and movement of contact lines, which can be triggered by van der Waals forces or the presence of roughness when the film becomes sufficiently thin. These situations are beyond the scope of the present paper.

It is worth noting that the present work suffers from a couple of limitations. First, the interfacial slopes were assumed small, or the film thickness should be sufficiently thin. It is not clear to what extent the results produced by lubrication theory are appropriate. Second, the values of Bo have been set not too large or small such that θ_d is not too close to 0 or π (figure 7), which ensures the zones can be well identified. For much larger values of Bo, our model may lack precision due to the employment of linearized curvature and the neglect of radial gravity component (Balestra *et al.* 2018). Furthermore, one may

expect Rayleigh–Taylor instabilities to occur in the region of the pendant drop (Pitts 1973, 1974). An examination of azimuthal effects based on three-dimensional models may also be of interest. These topics can be addressed by further experiments or direct numerical simulations, which will definitely help depict the more complicated film behaviours on spheres.

As a practical example, the present film configuration can be realized by dip coating of the sphere away from a liquid reservoir. While the initial film thickness may not be uniform, the presented features of film evolution at late stages are still helpful since they are expected to be insensitive to the initial conditions. Moreover, the present work can be extended to situations where the initial film is thick. The films in zones 1, 2 and 3 will eventually be sufficiently thin due to drainage and follow the same scaling laws presented in this work; zone 4 would be characterized by large surface slopes and hence should be handled by considering the balance between the hydrostatic pressure and the capillary force retaining the full curvature.

Acknowledgements

We acknowledge W. Lu for helpful discussions. This work was supported by NSFC (grant nos. 11672287, 11972340, 11932019 and 11621202), the Strategic Priority Research Program of the Chinese Academy of Sciences (grant no. XDB22040103) and the Fundamental Research Funds for the Central Universities.

Declaration of interests

The authors report no conflict of interest.

REFERENCES

BAKSHI, S., ROISMAN, I. V. & TROPEA, C. 2007 Investigations on the impact of a drop onto a small spherical target. *Phys. Fluids* **19**, 032102.

BALESTRA, G., NGUYEN, D. M.-P. & GALLAIRE, F. 2018 Rayleigh–Taylor instability under a spherical substrate. *Phys. Rev. Fluids* **3**, 084005.

BELOUSOV, A. P. & BELOUSOV, P. Y. 2010 Measuring the thickness of the fluid film moving on a spherical surface. *Optoelectron. Instrum. Proc.* **46**, 601–605.

BENILOV, E. S. & BENILOV, M. S. 2015 A thin drop sliding down an inclined plate. *J. Fluid Mech.* **773**, 75–102.

BENILOV, E. S., BENILOV, M. S. & KOPTEVA, N. 2008 Steady rimming flows with surface tension. *J. Fluid Mech.* **597**, 91–118.

BENILOV, E. S., CHAPMAN, S. J., MCLEOD, J. B., OCKENDON, J. R. & ZUBKOV, V. S. 2010 On liquid films on an inclined plate. *J. Fluid Mech.* **663**, 53–69.

BLAKE, T. D. & RUSCHAK, K. J. 1979 A maximum speed of wetting. *Nature* **282**, 489.

BONN, D., EGGERS, J., INDEKEU, J., MEUNIER, J. & ROLLEY, E. 2009 Wetting and spreading. *Rev. Mod. Phys.* **81**, 739–805.

BRAUN, R. J., USHA, R., MCFADDEN, G. B., DRISCOLL, T. A., COOK, L. P. & KING-SMITH, P. E. 2012 Thin film dynamics on a prolate spheroid with application to the cornea. *J. Engng Maths* **73**, 121–138.

DUPONT, T. F., GOLDSTEIN, R. E., KADANOFF, L. P. & ZHOU, S.-M. 1993 Finite-time singularity formation in Hele–Shaw systems. *Phys. Rev.* E **47**, 4182.

EMSLIE, A. G., BONNER, F. T. & PECK, L. G. 1958 Flow of a viscous liquid on a rotating disk. *J. Appl. Phys.* **29**, 858–862.

GAO, P., LI, L., FENG, J. J., DING, H. & LU, X.-Y. 2016 Film deposition and transition on a partially wetting plate in dip coating. *J. Fluid Mech.* **791**, 358–383.

DE GENNES, P.-G., BROCHARD-WYART, F. & QUÉRÉ, D. 2004 *Capillarity and Wetting Phenomena: Drops, Bubbles, Pearls and Waves*. Springer.

HECHT, F. 2012 New development in FreeFem++. *J. Numer. Math.* **20**, 251–265.

HOCKING, L. M. 1983 The spreading of a thin drop by gravity and capillarity. *Q. J. Mech. Appl. Maths* **36**, 55–69.

HOWELL, P. D. 2003 Surface-tension-driven flow on a moving curved surface. *J. Engng Maths* **45**, 283–308.

JALAAL, M., SEYFERT, C. & SNOEIJER, J. H. 2019 Capillary ripples in thin viscous films. *J. Fluid Mech.* **880**, 430–440.

KALLIADASIS, S., BIELARZ, C. & HOMSY, G. M. 2000 Steady free-surface thin film flows over topography. *Phys. Fluids* **12**, 1889–1898.

KANG, D., NADIM, A. & CHUGUNOVA, M. 2016 Dynamics and equilibria of thin viscous coating films on a rotating sphere. *J. Fluid Mech.* **791**, 495–518.

KANG, D., NADIM, A. & CHUGUNOVA, M. 2017 Marangoni effects on a thin liquid film coating a sphere with axial or radial thermal gradients. *Phys. Fluids* **29**, 072106.

KUMAR, S. 2015 Liquid transfer in printing processes: liquid bridges with moving contact lines. *Annu. Rev. Fluid Mech.* **47**, 67–94.

LAMSTAES, C. & EGGERS, J. 2017 Arrested bubble rise in a narrow tube. *J. Stat. Phys.* **167**, 656–682.

LEE, A., BRUN, P.-T., MARTHELOT, J., BALESTRA, G., GALLAIRE, F. & REIS, P. M. 2016 Fabrication of slender elastic shells by the coating of curved surfaces. *Nat. Commun.* **7**, 11155.

VAN LIMBEEK, M. A. J., SOBAC, B., REDNIKOV, A., COLINET, P. & SNOEIJER, J. H. 2019 Asymptotic theory for a Leidenfrost drop on a liquid pool. *J. Fluid Mech.* **863**, 1157–1189.

LOPES, A. B., THIELE, U. & HAZEL, A. L. 2018 On the multiple solutions of coating and rimming flows on rotating cylinders. *J. Fluid Mech.* **835**, 540–574.

MYERS, T. G., CHARPIN, J. P. F. & CHAPMAN, S. J. 2002 The flow and solidification of a thin fluid film on an arbitrary three-dimensional surface. *Phys. Fluids* **14**, 2788–2803.

PARKIN, I. P. & PALGRAVE, R. G. 2005 Self-cleaning coatings. *J. Mater. Chem.* **15**, 1689–1695.

PITTS, E. 1973 The stability of pendent liquid drops. Part 1. Drops formed in a narrow gap. *J. Fluid Mech.* **59**, 753–767.

PITTS, E. 1974 The stability of pendent liquid drops. Part 2. Axial symmetry. *J. Fluid Mech.* **63**, 487–508.

QUÉRÉ, D. 1999 Fluid coating on a fiber. *Annu. Rev. Fluid Mech.* **31**, 347–384.

REISFELD, B. & BANKOFF, S. G. 1992 Non-isothermal flow of a liquid film on a horizontal cylinder. *J. Fluid Mech.* **236**, 167–196.

ROY, R. V., ROBERTS, A. J. & SIMPSON, M. E. 2002 A lubrication model of coating flows over a curved substrate in space. *J. Fluid Mech.* **454**, 235–261.

SCHWARTZ, L. W. & WEIDNER, D. E. 1995 Modeling of coating flows on curved surfaces. *J. Engng Maths* **29**, 91–103.

SNOEIJER, J. H. & ANDREOTTI, B. 2013 Moving contact lines: scales, regimes, and dynamical transitions. *Annu. Rev. Fluid Mech.* **45**, 269–292.

SNOEIJER, J. H., ANDREOTTI, B., DELON, G. & FERMIGIER, M. 2007 Relaxation of a dewetting contact line. Part 1. A full-scale hydrodynamic calculation. *J. Fluid Mech.* **579**, 63–83.

SNOEIJER, J. H. & EGGERS, J. 2010 Asymptotic analysis of the dewetting rim. *Phys. Rev.* E **82**, 056314.

SNOEIJER, J. H., ZIEGLER, J., ANDREOTTI, B., FERMIGIER, M. & EGGERS, J. 2008 Thick films of viscous fluid coating a plate withdrawn from a liquid reservoir. *Phys. Rev. Lett.* **100**, 244502.

STILLWAGON, L. E. & LARSON, R. G. 1988 Fundamentals of topographic substrate leveling. *J. Appl. Phys.* **63**, 5251–5258.

STOCKER, R. & HOSOI, A. E. 2005 Lubrication in a corner. *J. Fluid Mech.* **544**, 353–377.

TAKAGI, D. & HUPPERT, H. E. 2010 Flow and instability of thin films on a cylinder and sphere. *J. Fluid Mech.* **647**, 221–238.

TANNER, L. H. 1979 The spreading of silicone oil drops on horizontal surfaces. *J. Phys.* D **12**, 1473.

WEINSTEIN, S. J. & RUSCHAK, K. J. 2004 Coating flows. *Annu. Rev. Fluid Mech.* **36**, 29–53.

WILD, J. D. & POTTER, O. E. 1972 A falling liquid film on a sphere. *Chem. Engng J.* **4**, 69–76.

WILSON, S. K., HUNT, R. & DUFFY, B. R. 2000 The rate of spreading in spin coating. *J. Fluid Mech.* **413**, 65–88.

XIA, Y., QIN, J. & GAO, P. 2020*a* Dynamical wetting transition on a chemically striped incline. *Phys. Fluids* **32**, 022101.

XIA, Y., QIN, J. & MU, K. 2020*b* Dynamics of moving contact line on a transversely patterned inclined surface. *Phys. Fluids* **32**, 042101.

ZHU, Y., LIU, H.-R., MU, K., GAO, P., DING, H. & LU, X.-Y. 2017 Dynamics of drop impact onto a solid sphere: spreading and retraction. *J. Fluid Mech.* **824**, R3.